Mechanism of the forward-angle (d,pn) reaction at intermediate energies

H. Okamura,[1,*] S. Ishida,[1,†] N. Sakamoto,[1,‡] H. Otsu,[1,§] T. Uesaka,[1,‡] T. Wakasa,[1,‖] H. Sakai,[1] T. Niizeki,[2,¶] H. Toyokawa,[2,**] Y. Tajima,[2,††] H. Ohnuma,[2,‡‡] M. Yosoi,[3] K. Hatanaka,[4] and T. Ichihara[5]

[1]*Department of Physics, University of Tokyo, Bunkyo-ku, Tokyo 113-0033, Japan*

[2]*Department of Physics, Tokyo Institute of Technology, Meguro-ku, Tokyo 152-8551, Japan*

[3]*Department of Physics, Kyoto University, Sakyo-ku, Kyoto 606-8502, Japan*

[4]*Research Center for Nuclear Physics, Osaka University, Ibaraki, Osaka 567-0047, Japan*

[5]*The Institute of Physical and Chemical Research (RIKEN), Saitama 351-0198, Japan*

(Received 23 March 1998)

The elastic breakup of the deuteron has been measured in a kinematical condition of $\theta_p=\theta_n=0°$ at $E_d=140$ MeV and 270 MeV on seven targets ranging from $Z=6$ to 82. A double-peaked structure with its minimum at $E_p\simeq E_n$ is observed for all the measured triple-differential cross sections, which indicates a large contribution from Coulomb breakup. While a symmetric shape is expected for an $E1$ transition, the observed proton-energy distribution is asymmetric, showing considerable dependence on both the target and the incident energy. These data and previous data at 56 MeV have been analyzed using the post-form of the distorted-wave Born approximation (DWBA) theory. Although the calculations account reasonably well for the asymmetric shape, by including the nuclear potential, they consistently overestimate the magnitudes of the cross sections over the whole measured region. Limitations of the post-form DWBA are discussed. [S0556-2813(98)03910-7]

PACS number(s): 24.10.−i, 24.50.+g, 25.45.De

I. INTRODUCTION

The breakup of unstable nuclei by the Coulomb interaction has recently attracted attention due to their astrophysical interest [1]. In order to extract relevant capture cross sections several reaction problems must be clarified. Particular uncertainties are the contributions from nuclear breakup and the ''post-acceleration'' effect arising from the different Coulomb potentials between the ejectiles and target. Various theoretical models, such as the semiclassical coupled-channels approach [2,3], the direct numerical integration of the time-dependent Schrödinger equation [4,5], the sudden approximation [6], the post-formalism of the distorted-wave Born approximation (DWBA) [7], and most recently a three-body adiabatic formulation [11], have been proposed for treating such problems. The low intensity currently available for unstable nuclei, however, leads to limited data having large uncertainties which effectively hampers the challenge to these theoretical descriptions.

The study may be efficiently pursued by using light-ion primary beams. Because of its small breakup-energy and the dominance of the S wave in the ground state, the deuteron can be considered as the simplest example of an ''exotic'' nucleus. There is no ambiguity in the projectile wave function and the absence of resonances certifies the direct breakup mechanism. Besides, the post-acceleration effect is strongly enhanced in deuteron breakup where the entire projectile charge is carried by one of the ejectiles having only half of the total mass.

Although the breakup of the deuteron has been the subject of extensive investigations, few data exist which manifest the Coulomb breakup, particularly at energies above the Coulomb barrier. In our previous study at 56 MeV [8], a strong indication of Coulomb breakup was first observed at $\theta_p=\theta_n=0°$, yet a considerable influence of distortion was suggested at the same time. Measurements at intermediate energies ($E_d>100$ MeV), where the distortion becomes smaller, are highly desirable, but have never been done because facilities capable of providing such a beam were rare until recently. In this paper, data for the elastic breakup of 140 and 270 MeV deuterons at $\theta_p=\theta_n=0°$ are presented and analyzed along with the data at 56 MeV. The implications of these previous data are discussed by some authors, but only qualitatively [9] or even misleadingly [10]. It is also an object of this paper to present a rigorous calculation including a way to make a comparison with the data.

The experimental procedure and results are given in Secs. II and III, respectively. The analysis based on the post-form DWBA and its possible implications are given in Secs. IV and V, respectively. A part of the data has been presented elsewhere [11] together with an analysis based on the new

*Present address: Department of Physics, Saitama University, Saitama 338-8570, Japan. Electronic address: okamura@phy.saitama-u.ac.jp

†Present address: Soei International Patent Firm, Tokyo 104-0031, Japan.

‡Present address: The Institute of Physical and Chemical Research (RIKEN), Saitama 351-0198, Japan.

§Present address: Department of Physics, Tohoku University, Sendai 980-8578, Japan.

‖Present address: Research Center for Nuclear Physics, Osaka University, Osaka 567-0047, Japan.

¶Present address: Department of Home Economics, Tokyo Kasei University, Tokyo 173-8602, Japan.

**Present address: Japan Synchrotron Radiation Research Institute (JASRI), Akou 678-1298, Japan.

††Present address: Cyclotron and Radioisotope Center, Tohoku University, Sendai 980-8578, Japan.

‡‡Present address: Chiba Institute of Technology, Narashino, Chiba 275-8588, Japan.

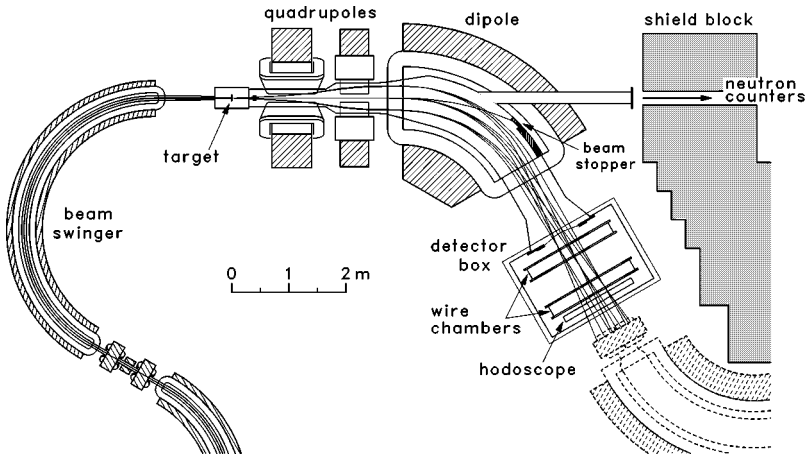

FIG. 1. Schematic view of the experimental setup. Protons are detected at the first focal plane of the spectrograph SMART, making the most of its large momentum acceptance. Trajectories of protons, as well as the deuteron beam which has twice the magnetic rigidity as that of protons, are also shown.

approach to the Coulomb breakup process. As stated there, that method is not immediately applicable to the treatment of nuclear breakup. In the present analysis, the nuclear interaction is treated on the same footing as the Coulomb interaction but employing the conventional zero-range DWBA.

II. EXPERIMENTAL PROCEDURE

The (d,pn) elastic breakup reaction, which leaves the target nucleus in its ground state, has been measured at the RIKEN Accelerator Research Facility in a kinematical condition of $\theta_p = \theta_n = 0°$. Deuteron beams of 140 MeV and 270 MeV, provided by the ring cyclotron, were used to bombard the targets ^{12}C, ^{28}Si, ^{40}Ca, ^{90}Zr, ^{118}Sn, ^{165}Ho, and ^{208}Pb, which were all self-supporting foils of natural or isotopically enriched elements. Protons emitted were momentum analyzed by using the spectrograph SMART [12] and measured by a pair of multiwire drift chambers followed by a plastic scintillator hodoscope equipped at the first focal plane (Fig. 1). Details of the charged-particle detection system, as well as the properties of the spectrograph, can be found elsewhere [13]. Neutrons were detected by two (six) sets of NE213 liquid scintillation counters at a distance of 12 m (22 m) from the target for the 140 MeV (270 MeV) incident energy. Background γ and cosmic rays were eliminated by using the pulse-shape discrimination method. Charged particles were rejected by thin plastic scintillation counters placed in front of the neutron counters. The neutron energy was determined by the time-of-flight method. The resolution of the total energy $E_p + E_n$ was 2.5 MeV [full width at half maximum (FWHM)] or better depending on the target. Typical coincidence energy spectra are shown in Fig. 2. The solid angles of the neutron and proton detectors, which are shown to have importance in Sec. IV, are listed in Table I.

The incident beam, having twice the magnetic rigidity as that of the protons measured, was stopped inside the dipole magnet of the spectrograph (Fig. 1). The yoke of the dipole magnet thus served as a shield, allowing the low-background measurement. It should be noted that the situation is very different for measurements at angles other than zero degrees, where the incident beam has to be stopped inside the scattering chamber and it is then difficult to shield the background neutrons produced near the target. Only very limited data have been obtained at larger angles in the present experiment. The beam intensity was kept weak, typically 0.01–0.4 nA, to make the accidental coincidence background reason-

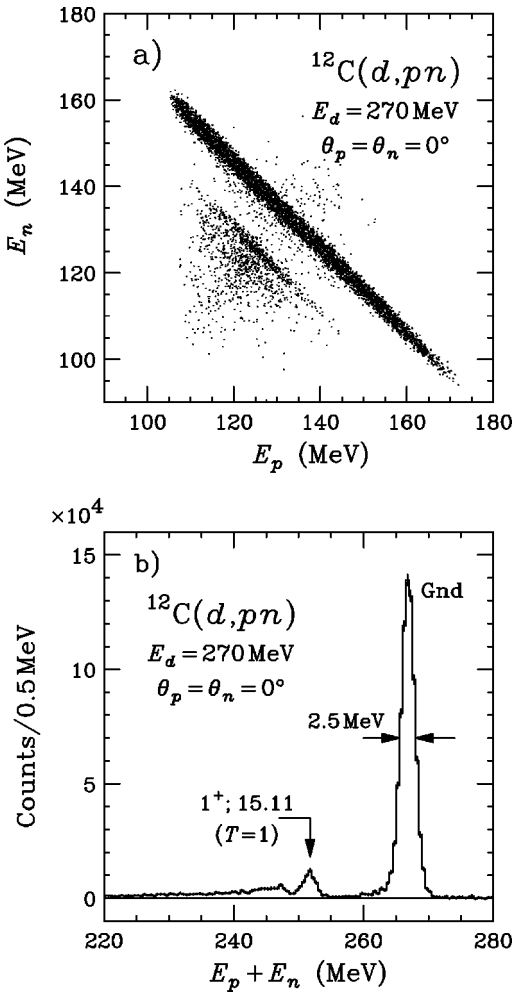

FIG. 2. (a) Two-dimensional and (b) summed energy spectra of the coincidence protons and neutrons from the deuteron breakup on the ^{12}C target at 270 MeV. The effects of accidental coincidence are corrected for.

TABLE I. Solid angles of the neutron and proton detectors.

E_d (MeV)	$\Delta\Omega_n$ (msr)[a]	$\Delta\Omega_p$ (mrad^2)
140	0.45	60×120
270	0.48	60×120
56[b]	0.88	75×75

[a]Circular shape.
[b]Taken from Ref. [8].

ably small. The contribution from the electric dark current in the beam stopper, which was not negligible compared with the beam intensity, was eliminated by using a monitor counter.

The neutron detection efficiency was calibrated using the ^{7}Li$(p,n)^7$Be[g.s.+0.43 MeV] reaction [14] at E_p = 70 MeV and 135 MeV [Fig. 3(a)]. The proton beam was obtained by accelerating H_2^+, the singly charged hydrogen molecule, with the same cyclotron field as that for the deuteron in order to minimize the time lag between the calibration and the breakup measurement. The energy dependence of the detection efficiency was extrapolated by using a Monte Carlo calculation [15] which, as shown in Fig. 3(b), is almost flat in the region relevant to the present measurement. The optics property of the spectrograph was also studied by using protons elastically scattered from a gold target. The systematic error, including those arising from uncertainties of the beam intensity and the target thickness, is estimated to be 30%.

Because of the lack of available optical potentials, the elastic scattering was also measured at 140 MeV on ^{12}C, ^{40}Ca, and ^{208}Pb targets at the second focal plane of SMART where a better momentum and angular resolution is achieved. Details of the measurement of elastic scattering will be described elsewhere.

III. RESULTS

The measured triple-differential cross sections at $\theta_p = \theta_n = 0°$ are presented in Figs. 4 and 5 for E_d = 140 MeV and 270 MeV, respectively, plotted as a function of the detected

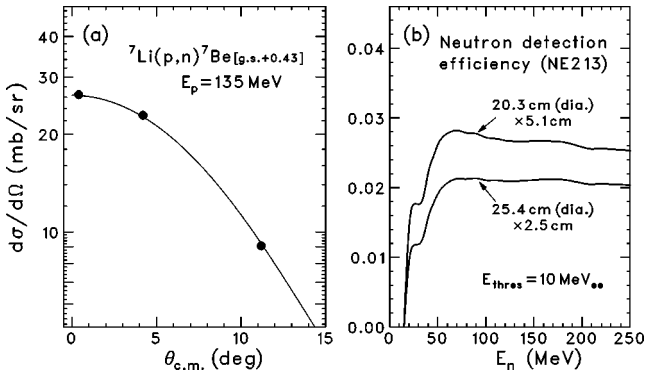

FIG. 3. (a) Typical angular distribution of the ^{7}Li$(p,n)^7$Be[g.s.+0.43 MeV] reaction obtained by using 270 MeV H_2^+. It is normalized to the Fourier-Bessel representation given in Ref. [14] (solid curve) for calibrating the neutron detection efficiency. (b) The energy dependence of the detection efficiency calculated by a Monte Carlo code [15] for the neutron counters used in the present experiment.

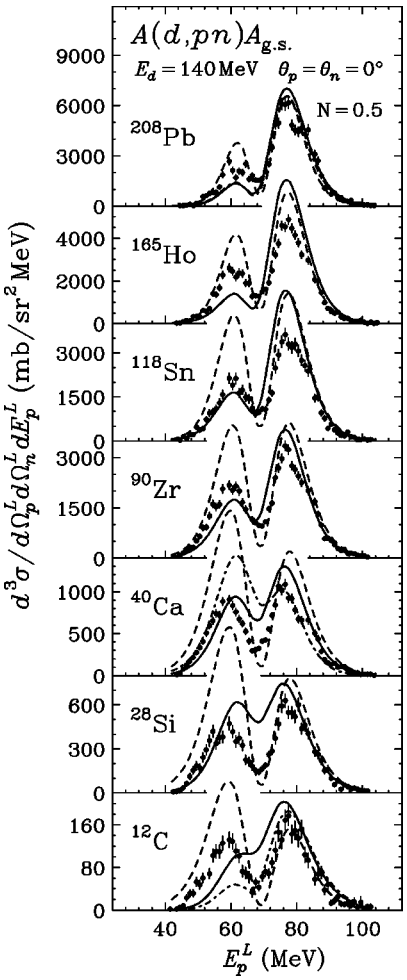

FIG. 4. Triple-differential cross sections for the elastic breakup of 140-MeV deuterons at $\theta_p = \theta_n = 0°$ on the ^{12}C, ^{28}Si, ^{40}Ca, ^{90}Zr, ^{118}Sn, ^{165}Ho, and ^{208}Pb targets. The results of the post-form DWBA calculation using the potential sets A (solid curves) and B (dot-dashed curves) in Table II are presented but commonly multiplied by a factor of 0.5. The result of the pure-Coulomb calculation is also shown (dashed curves) without any normalization. The calculated cross sections are averaged over the solid angles of the detectors. See text for details.

proton energy. Because of the difficulty described in the previous section, the data at larger angles have been obtained only on the ^{12}C target at 270 MeV for $\theta_p^L = \theta_n^L$ which are shown in Fig. 6. All the cross sections are presented in the laboratory frame. The errors shown in figures are the statistical ones only.

A common feature of the proton-energy spectra at $\theta = 0°$ is a double-peaked structure with its minimum at $E_p \simeq \frac{1}{2}E_d$. They are significantly different from the bell-shaped spectra shown in the lower panels of Fig. 6 and usually observed at backward angles. The shape of the spectrum is symmetric for light targets at 270 MeV but becomes asymmetric, showing an enhancement of the higher-proton-energy peak, as the target mass increases. The degree of asymmetry becomes even larger at lower incident energies. For the data at 56 MeV, which were obtained previously [8] and are shown in Fig. 7, the data reduce to almost a single peak for ^{208}Pb.

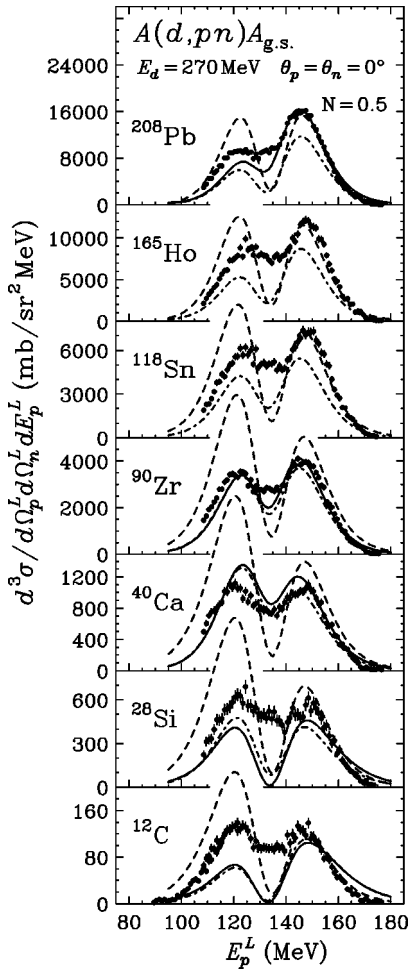

FIG. 5. Same as Fig. 4 but for $E_d = 270$ MeV. The potential sets in Table III are used for calculations.

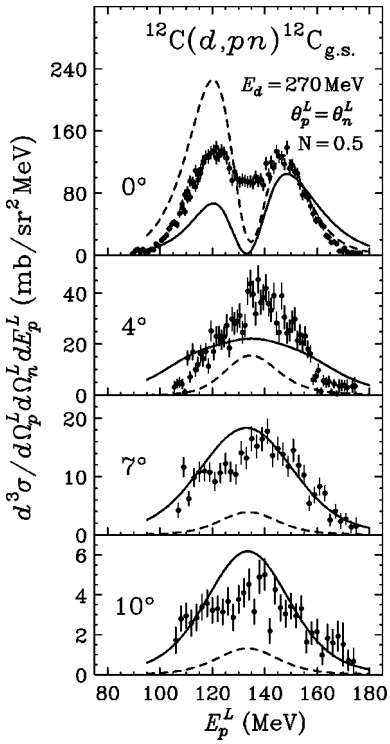

FIG. 6. Triple-differential cross sections for the ^{12}C$(d,pn)^{12}$C$_{g.s.}$ reaction at $E_d = 270$ MeV and at $\theta_p^L = \theta_n^L = 0°$, 4°, 7°, and 10°. The meanings of the solid and dashed curves are the same as those in Fig. 5.

The gross evolution of the cross sections is illustrated in Fig. 8(a) where the energy-integrated double-differential cross section is shown for each incident energy, plotted as a function of the atomic number Z of the target. The data at 270 MeV are on a straight line (on a logarithmic scale) close to Z^2 and therefore indicate the dominance of Coulomb breakup. As the incident energy goes down, however, the cross section tends to be suppressed for heavy targets, resulting in the characteristic behavior at 56 MeV where the maximum is observed at $Z \simeq 20$. A strong influence on the distorted waves is suggested by this Z dependence as well as the asymmetric shape of the spectrum.

IV. ANALYSIS

As discussed in a previous study [8], the origin of the double peak is readily understood on the basis of the prior formalism of the DWBA, the T matrix of which is expressed as [16]

$$T_{\rm prior} = \langle \psi_{d*}^{(-)} \chi_{d*A}^{(-)} | V_{pA} + V_{nA} - V_{dA} | \phi_d \, \chi_{dA}^{(+)} \rangle , \qquad (1)$$

where ϕ_d and ψ_{d*} denote the bound and scattering states of the p-n system, respectively, and V_{iA} and χ_{iA} denote the potential and the distorted wave between the particle i and the target, respectively. For pure-Coulomb breakup, i.e., $V_{pA} + V_{nA} - V_{dA} \rightarrow Ze^2(r_{pA}^{-1} - r_{dA}^{-1})$, and using an explicit representation of the p-n wave functions,

$$\phi_d = \sum_j c_j e^{-\alpha_j r_{pn}}/r_{pn} , \quad \psi_{d*}^{(+)} = e^{i\mathbf{k}_{pn}\cdot\mathbf{r}_{pn}} ,$$

where $\mathbf{k}_{pn}$ is the p-n relative momentum, $T_{\rm prior}$ is reduced to

$$T_{\rm prior}^{E1} = \sum_j \frac{i4\pi Z e^2 c_j}{(\alpha_j + k_{pn}^2)^2} \left\langle \chi_{d*A}^{(-)} \left| \frac{\mathbf{k}_{pn}\cdot\mathbf{r}_{dA}}{r_{dA}^3} \right| \chi_{dA}^{(+)} \right\rangle , \qquad (2)$$

if the dipole approximation is well fulfilled. Since Eq. (2) becomes zero at $k_{pn} = 0$ where $E_p = E_n \simeq \frac{1}{2} E_d$, the double peak observed in the experimental spectra also strongly suggests the dominance of the Coulomb breakup.

$T_{\rm prior}^{E1}$ gives only symmetric spectra. The asymmetric shape can arise from interference with nuclear breakup and from the higher-order effects (than $E1$) of the unbalanced Coulomb potentials in the final state. These however are treated only perturbatively in Eq. (1) and, in addition, there is no way to describe χ_{d*A} properly [17]. The prior-form DWBA is likely to be a poor approximation, although the rapid convergence with respect to p-n partial waves makes it attractive for numerical evaluations.

The post-form DWBA, on the other hand, should describe the asymmetric shape better if it is mainly caused by the unbalanced Coulomb distortions, which are properly treated in the T matrix [16]:

$$T_{\rm post} = \langle \chi_{pA}^{(-)} \chi_{nB}^{(-)} | V_{pn} + V_{nA} - V_{nB} | \phi_d \, \chi_{dA}^{(+)} \rangle , \qquad (3)$$

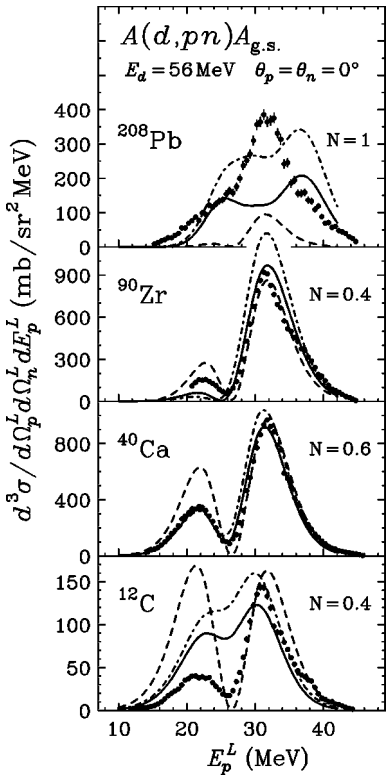

FIG. 7. Same as Fig. 4 but for $E_d = 56$ MeV and on the ^{12}C, ^{40}Ca, ^{90}Zr, and ^{208}Pb targets (taken from Ref. [8]). The calculations using the potential sets A (solid curves) and B (dot-dashed curves) in Table IV are presented multiplied by the factors shown in the figure.

where B denotes the $p+A$ system. Since quantities appearing in Eq. (3) are determined less ambiguously than those in $T_{\rm prior}$, $T_{\rm post}$ is expected to be a good approximation also for the treatment of nuclear potentials. In this paper, an analysis based on the post-form DWBA is presented and compared with the new data and the previous data at 56 MeV [8]. Details of the calculation, including a useful technique which led us to employ this approximation for the present case, are described in the Appendix. It is worth noting that the present calculation is a conventional one, treating the nuclear interaction on the same footing as the Coulomb interaction, and differs distinctly from the method of Ref. [7] where the effects of nuclear interactions are incorporated using a diffraction dissociation theory.

The distorted wave is produced by an optical potential with the standard form

$$V(r) = -V_R f(r_R, a_R; r) - iW_V f(r_I, a_I; r) + i4a_I W_D \frac{d}{dr} f(r_I, a_I; r) + V_{\rm Coulomb},$$

where

$$f(r_i, a_i; r) = \left[1 + \exp\left(\frac{r - r_i A^{1/3}}{a_i}\right)\right]^{-1}.$$

The parameters used in the calculations at 140 MeV, 270 MeV, and 56 MeV are listed in Tables II, III, and IV, respectively. The Coulomb radius r_C is fixed as 1.3 fm. Since calculations have to be made over a wide range of proton and neutron energies, energy-dependent global parametrizations are employed for the available cases. At intermediate energies, the deuteron optical potentials are available only for very limited cases. All the parameters used in the present analysis are deduced from the measurements at RIKEN. Figure 9 shows the deuteron elastic scattering at 140 MeV with the optical-model fits obtained using the code ECIS79 [28]. The 270 MeV data are taken from Refs. [21,22]. As well as these experimentally obtained potentials, those deduced from nucleon optical potentials, according to the method of Johnson and Soper [18], are used for comparison as well as to see the systematic dependence on the target. These potentials are referred to as sets A and B in Tables II–IV. Pure-Coulomb calculations given by Eq. (A2) are also presented to clarify the effect of the nuclear potentials.

The triple-differential cross section is obtained by

$$\frac{d^3\sigma}{d\Omega_p^L d\Omega_n^L dE_p^L} = \frac{2\pi\mu_{dA}}{\hbar^2 k_{dA}} |T|^2 \rho,$$

where ρ is the phase-space distribution with respect to Ω_p^L, Ω_n^L, and E_p^L [29]. In the following, the experimental data are compared with the averaged cross section,

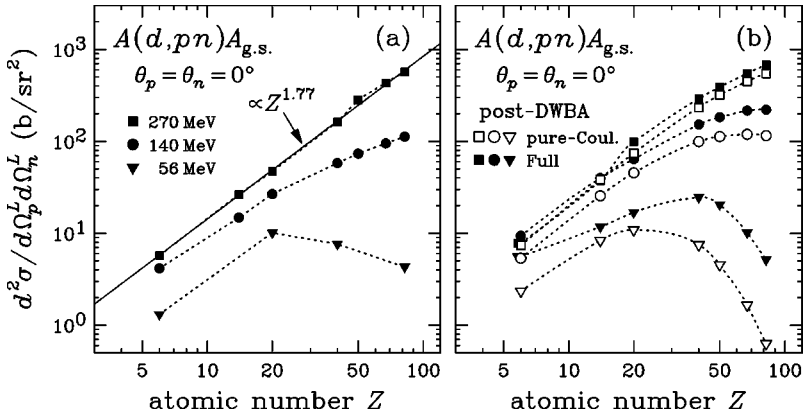

FIG. 8. Dependence of the energy-integrated cross section on the atomic number Z of the target (a) for the present data along with the previous ones [8] and (b) for the corresponding post-form DWBA calculations. The pure-Coulomb calculation and the one using the potential deduced by the Johnson-Soper method [18] are presented by the open and solid symbols, respectively, without any normalization.

TABLE II. Optical-potential parameters used for the analysis of 140-MeV data.

		Set	V_R (MeV)	r_R (fm)	a_R (fm)	W_V (MeV)	W_D (MeV)	r_I (fm)	a_I (fm)	Ref.
^{12}C	*d*	A	49.39	1.23	0.77	5.73	3.70	1.45	0.48	[a]
	d	B	54.80	1.29	0.70	6.99	3.85	1.48	0.60	[b]
	p,n		25.39	1.244	0.712	2.84	2.32	1.469	0.39	[19]
^{28}Si	*d*	A	76.23	1.10	0.80	14.41	5.89	1.28	0.58	[a]
	p,n		38.63	1.116	0.739	7.18	3.46	1.288	0.507	[19]
^{40}Ca	*d*	A	71.38	1.17	0.75	12.55	6.53	1.20	0.75	[a]
	d	B	36.17	1.38	0.79	1.07	9.46	0.97	0.94	[b]
	p,n		35.83	1.18	0.69	6.23	3.61	1.21	0.69	[20]
^{90}Zr	*d*	A	77.10	1.19	0.75	11.76	8.52	1.23	0.76	[a]
	p,n		38.56	1.20	0.69	5.87	4.65	1.24	0.69	[20]
^{118}Sn	*d*	A	79.27	1.20	0.75	11.41	9.35	1.24	0.76	[a]
	p,n		39.63	1.20	0.69	5.70	5.09	1.24	0.69	[20]
^{165}Ho	*d*	A	81.88	1.20	0.75	10.84	10.27	1.25	0.76	[a]
	p,n		40.93	1.21	0.69	5.42	5.59	1.25	0.69	[20]
^{208}Pb	*d*	A	83.85	1.21	0.75	10.38	10.96	1.25	0.76	[a]
	d	B	60.56	1.20	0.85	20.99	1.92	1.16	1.25	[b]
	p,n		41.91	1.21	0.69	5.19	5.97	1.26	0.69	[20]

[a]Deduced from nucleon optical potentials according to Ref. [18].
[b]Obtained in the present analysis (Fig. 9).

TABLE III. Same as Table II but for 270 MeV. E=laboratory energy and $W_D=0$.

		Set	V_R (MeV)	r_R (fm)	a_R (fm)	W_V (MeV)	r_I (fm)	a_I (fm)	Ref.
^{12}C	*d*	A	20.1	1.43	0.74	53.9	0.87	0.73	[21]
	d	B	25.5	1.37	0.59	45.1	0.84	0.73	[a]
	p,n		12.84	1.40	0.515	25.4	0.805	0.71	[23]
^{28}Si	*d*	A	23.3	1.25	0.80	54.14	0.93	0.98	[22]
	d	B	24.8	1.37	0.63	32.2	1.04	0.80	[a]
	p,n		12.40	1.39	0.55	16.4	1.05	0.75	[23]
^{40}Ca	*d*	A	28.8	1.37	0.79	27.9	1.18	0.74	[21]
	d	B	42.7	1.25	0.78	17.5	1.31	0.72	[a]
	p,n		105.5	1.125	0.675	[b]	1.65	0.32	[24]
			$-17.14\ln E$	$+0.001E$	$+0.00031E$		$-0.0024E$	$+0.0025E$	
^{90}Zr	*d*	A	32.4	1.35	0.74	31.4	1.22	0.73	[21]
	d	B	46.5	1.25	0.78	17.5	1.32	0.72	[a]
	p,n		107.3	[c]	0.675	[b]	1.65	0.32	[24]
			$-17.14\ln E$		$+0.00031E$		$-0.0024E$	$+0.0025E$	
^{118}Sn	*d*	B	47.8	1.25	0.78	17.5	1.32	0.72	[a]
	p,n		108.0	[b]	0.675	[b]	1.65	0.32	[24]
			$-17.14\ln E$		$+0.00031E$		$-0.0024E$	$+0.0025E$	
^{165}Ho	*d*	B	49.0	1.25	0.78	17.5	1.32	0.72	[a]
	p,n		108.6	[c]	0.675	[b]	1.65	0.32	[24]
			$-17.14\ln E$		$+0.00031E$		$-0.0024E$	$+0.0025E$	
^{208}Pb	*d*	A	22.6	1.35	0.75	13.7	1.28	0.66	[21]
	d	B	49.4	1.25	0.78	17.5	1.32	0.72	[a]
	p,n		109.0	[c]	0.675	[b]	1.65	0.32	[24]
			$-17.14\ln E$		$+0.00031E$		$-0.0024E$	$+0.0025E$	

[a]Deduced from nucleon optical potentials according to Ref. [18].
[b]$6.6+2.73\times10^{-2}(E-80)+3.87\times10^{-6}(E-80)^3$.
[c]$\min(1.255, 1.125+0.001E)$.

TABLE IV. Same as Table II but for 56 MeV. E=laboratory energy.

		Set	V_R (MeV)	r_R (fm)	a_R (fm)	W_V (MeV)	W_D (MeV)	r_I (fm)	a_I (fm)	Ref.
^{12}C	d	A	79.79	1.12	0.742	0.0	11.55	1.23	0.666	[25]
	d	B	103.62	1.10	0.637	1.28	13.33	1.11	0.579	[a]
	p,n		61.05 $-0.277E$	1.15 $-0.001E$	0.57	[b]	9.60 $-0.055E$	1.15 $-0.001E$	0.50	[26]
^{40}Ca	d	A	75.47	1.20	0.769	2.452	9.775	1.32	0.783	[25]
	d	B	94.19	1.16	0.810	8.08	9.43	1.27	0.631	[a]
	p		56.34 $-0.32E$	1.17	0.75	-2.7 $+0.22E$	11.8 $-0.25E$	1.32	0.51	[27]
	n		56.30 $-0.32E$	1.17	0.75	-1.56 $+0.22E$	13.0 $-0.25E$	1.26	0.58	[27]
^{90}Zr	d	A	89.16	1.11	0.816	5.034	8.289	1.36	0.786	[25]
	d	B	95.89	1.16	0.810	8.03	9.45	1.29	0.668	[a]
	p		60.24 $-0.32E$	1.17	0.75	-2.7 $+0.22E$	13.1 $-0.25E$	1.32	0.588	[27]
	n		53.63 $-0.32E$	1.17	0.75	-1.56 $+0.22E$	11.67 $-0.25E$	1.26	0.58	[27]
^{208}Pb	d	A	88.60	1.17	0.768	4.201	10.30	1.27	0.891	[25]
	d	B	97.94	1.16	0.808	8.01	9.41	1.29	0.720	[a]
	p		64.61 $-0.32E$	1.17	0.75	-2.7 $+0.22E$	14.4 $-0.25E$	1.32	0.658	[27]
	n		51.22 $-0.32E$	1.17	0.75	-1.56 $+0.22E$	10.46 $-0.25E$	1.26	0.58	[27]

[a]Deduced from nucleon optical potentials according to Ref. [18].
[b]$\max(0, \min(7.5, 1.06E-37.6))$.

$$\left\langle \frac{d^3\sigma_{\rm calc}}{d\Omega_p^L d\Omega_n^L dE_p^L} \right\rangle = \frac{1}{\Delta\Omega_p \Delta\Omega_n} \times \int_{\Delta\Omega_p\Delta\Omega_n} d\Omega_p^L d\Omega_n^L \frac{d^3\sigma_{\rm calc}}{d\Omega_p^L d\Omega_n^L dE_p^L},$$

where the integration is carried out over the solid angles of the proton ($\Delta\Omega_p$) and neutron ($\Delta\Omega_n$) detectors (Table I). Since $\Delta\Omega_n$ is small, an integration only on $\Delta\Omega_p$ gives an almost identical result. The average must be taken because the calculated angular distribution near 0° is extremely steep and exhibits complex behavior. For example, Fig. 10 shows the dependence of the triple-differential cross section on the proton angle θ_p^L for several targets at 140 MeV with the neutron angle fixed at 0°. It is remarkable that the maximum point of the cross section moves from $\theta=0°$ for heavy targets. As the proton detector covers θ_p^L up to 3.5° around 0°, the averaged cross section is likely to be different in magnitude as well as in shape from the one calculated exactly at 0°. The situation is essentially the same for the pure-Coulomb calculation. It is worth noting that, while it has not been studied in the present experiment due to the lack of resolution, a detailed angular distribution was reported from IUCF on carbon and copper targets at $E_d=260$ MeV [30] where, without using a spectrograph, a good angular resolution was achieved but at the sacrifice of the energy resolution.

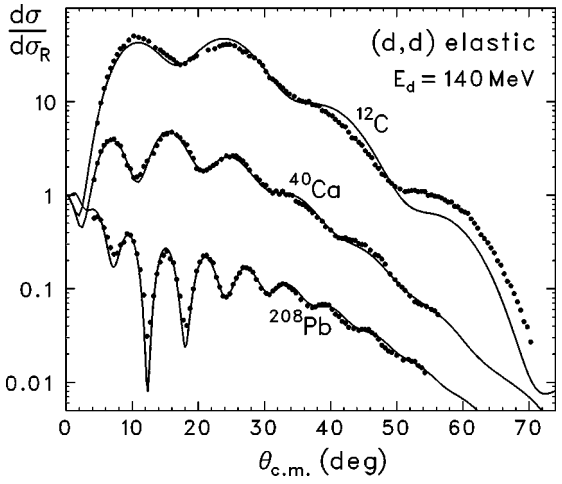

FIG. 9. Angular distributions and the optical-model fits for the elastic scattering cross section at 140 MeV on the ^{12}C, ^{40}Ca, and ^{208}Pb targets.

The results of calculations are shown in Figs. 4–8 and 11. Except for Fig. 8(b), the solid and dot-dashed curves represent the calculations using the potential sets A and B for the corresponding tables, respectively, multiplied by the factors indicated in the figures (mostly 0.5). The dashed curves represent the pure-Coulomb calculations without normalization. In Fig. 8(b) the calculations with and without nuclear potentials are presented by solid and open symbols, respectively. It should be noted that the averaged cross section has moderate target dependence in spite of its complicated angular distribution as a consequence of the specific choice of the detector solid angles.

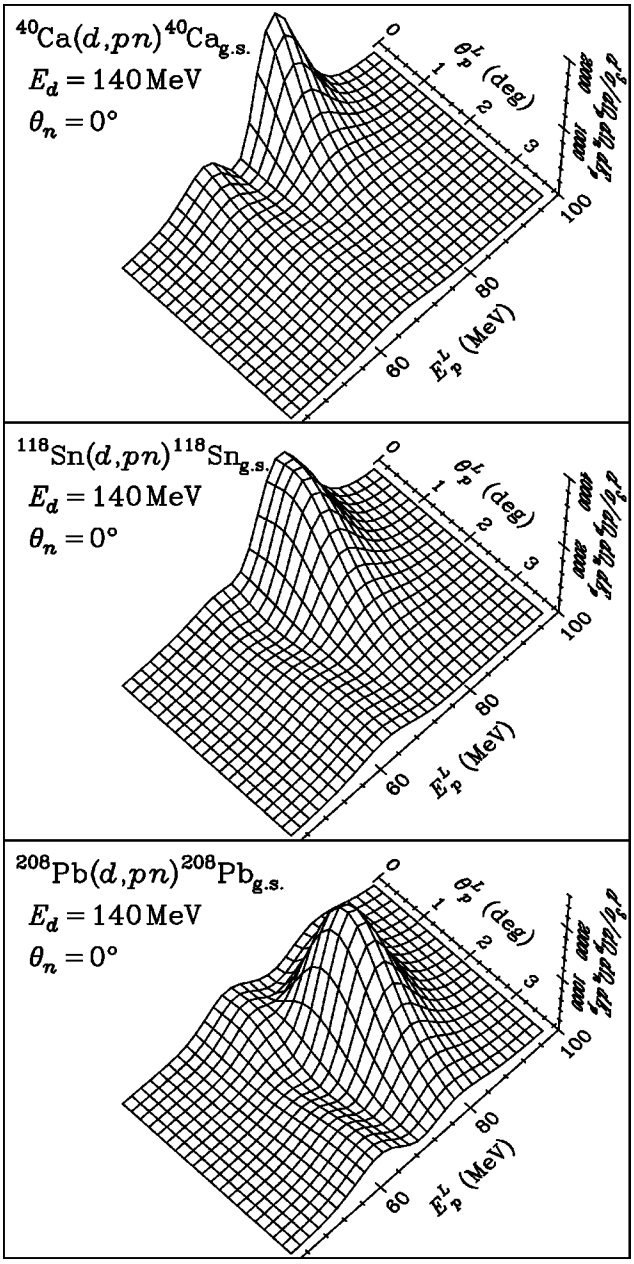

FIG. 10. Calculated triple-differential cross sections at $E_d = 140$ MeV for the ^{40}Ca, ^{165}Ho, and ^{208}Pb targets plotted as a function of the proton angle θ_p^L. The neutron angle is fixed at $\theta_n = 0°$ and the potential set A in Table IV is used.

Considering the systematic uncertainty of the experiment, the magnitudes of the cross sections are reasonably well reproduced by the pure-Coulomb calculations, except for the ^{208}Pb target at 56 MeV (Fig. 7) and for the backward angles (Figs. 6 and 11) where the nuclear interaction is likely to have a larger contribution. Concerning the shape of the proton-energy spectra, however, the agreement is rather poor. Although the double peak is produced at $\theta = 0°$ for all targets and incident energies, the lower-energy peak in the spectrum tends to be overestimated. The discrepancy becomes significant, particularly for light targets (Figs. 4, 5, and 7).

By including the nuclear potentials, the lower-energy peak is relatively suppressed and also the minimum of the double peak tends to be filled, resulting in improved agreement with the data. The spectrum shape is remarkably well reproduced for heavy targets at 140 and 270 MeV and for ^{40}Ca at 56 MeV (Figs. 4, 5, and 7). However, the magnitude of the cross section is consistently overestimated and about twice as large as the data. The difference between the calculations using the deuteron optical potential and the one deduced by the Johnson-Soper method [18] is generally small both in shape and in magnitude. A distinct change between the ^{40}Ca and ^{28}Si targets at 270 MeV [Figs. 5 and 8(b)] can be attributed to the difference in the nucleon optical potentials between the energy-dependent global parametrization for $A \geqslant 40$ [24] and the parameters at $E_p = 156$ MeV [23] used for $A < 40$.

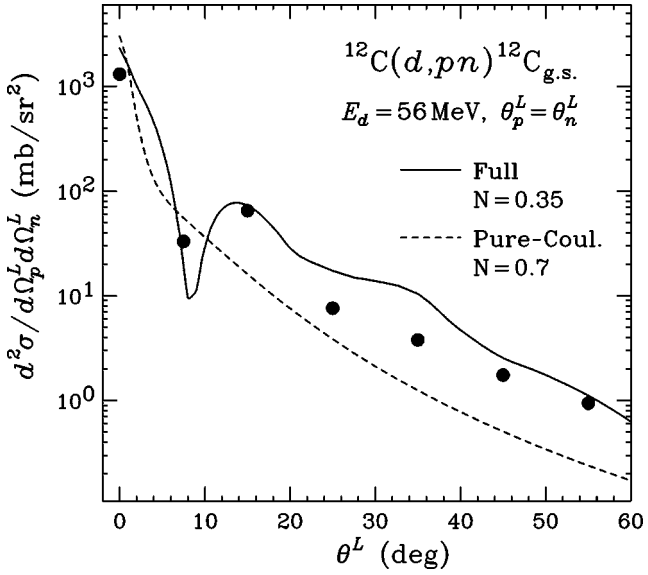

FIG. 11. Angular distribution of the energy-integrated cross section for the ^{12}C$(d,pn)^{12}$C$_{g.s.}$ reaction at $E_d = 56$ MeV (taken from Refs. [8,31]). The results of the calculation using the potential set A in Table IV multiplied by a factor of 0.5 and of the pure-Coulomb calculation are presented by the solid and dashed curves, respectively. The calculated cross sections are averaged over the solid angles of the detectors.

Unfortunately angular distributions are available only for the ^{12}C target where the present approximation is expected to be invalid (cf. the Appendix). Nevertheless, the increasing contribution from nuclear breakup at backward angles is worth noting. At $E_d = 270$ MeV, while the pure-Coulomb calculation severely underestimates the cross section at angles other than 0°, the one including nuclear potentials gives better agreement with the data, not only for the magnitude of the cross section, but also for the broad bell shape of the spectra at $\theta^L = 7°$ and 10° (Fig. 6). The spectrum at $\theta^L = 4°$, where the nuclear breakup contribution is of the same order as the Coulomb breakup, thus producing a complicated interference effect, is poorly reproduced. It should be noted that, although k_{pn} can be close to zero in the geometry of $\theta_p^L = \theta_n^L$, the post-form pure-Coulomb calculation gives bell-shaped distributions at θ^L other than 0° (dashed curves in Fig. 6) unlike the simple $E1$ transition [Eq. (2)] which gives a double-peaked distribution at any angles. At $E_d = 56$ MeV, the diffractive angular distribution is fairly well reproduced by including the nuclear potentials, although the magnitude is consistently overestimated (Fig. 11).

V. DISCUSSION

Considering the remarkable success of the post-form DWBA at backward angles and below 56 MeV (cf. Fig. 14 and Refs. [16,37]), the present failure in reproducing the magnitude of the cross section is surprising. As described in the Appendix, the validity of the approximations, $V_{nA} \simeq V_{nB}$ and $V_{pn}\phi_d \simeq D_0\,\delta(\mathbf{r}_{pn})$, introduced to the original form of $T_{\rm post}$ [Eq. (3)] is a point at issue. But they do not necessarily deteriorate the description in the particular geometry of $\theta_p=\theta_n=0°$.

The p-n final state interaction (FSI), on the other hand, which is treated only perturbatively in the post-form DWBA, surely plays an important part at forward angles. It is more clearly illustrated in the prior-form DWBA. In the limit of the plane-wave approximation, Eq. (1) is reduced to

$$T^{\rm PW}_{\rm prior}=\langle \psi^{(-)}_{d*}|e^{i\mathbf{q}\cdot\mathbf{r}_{pn}/2}|\phi_d\rangle \overline{V}(\mathbf{q}),$$

where $\overline{V}$ denotes the Fourier transform of $V_{pA}+V_{nA}$ (V_{dA} does not contribute to the reaction) and $\mathbf{q}$ is the momentum transfer. At forward angles where $\mathbf{q}\simeq 0$, $T^{\rm PW}_{\rm prior}$ becomes close to zero due to the orthogonality relation $\langle\psi_{d*}|\phi_d\rangle=0$. In other words, noting the decomposition $\psi^{(+)}_{d*}=\exp(i\mathbf{k}_{pn}\cdot\mathbf{r}_{pn}) + \psi^{(+)}_{\rm FSI}$, the FSI amplitude $\langle\psi^{(-)}_{\rm FSI}|V|\phi_d\rangle$ destructively interferes with the quasifree scattering (QFS) amplitude $\langle e^{-i\mathbf{k}_{pn}\cdot\mathbf{r}_{pn}}|V|\phi_d\rangle$. Since ϕ_d is mainly in the $^3S_1$ state, $\psi_{\rm FSI}$ also mainly consists of the S wave. Accordingly the FSI amplitude has a bell-shaped distribution and reduces the cross section across a broad range of the proton energy. The overestimate of the cross section in the present analysis therefore can be attributed to the improper treatment of the p-n FSI in the post-form DWBA. It should be noted that $\psi_{\rm FSI}$ hardly contributes to the Coulomb breakup which is primarily caused by the dipole excitation. This qualitatively explains the present situation where the pure-Coulomb calculation better reproduces the magnitude of the cross section.

As we employ the zero-range approximation, it is difficult to incorporate the p-n FSI amplitude in the present calculation. Besides the study of projectile dependence is practically impossible because the projectile information is in principle reduced to a factor D_0. Nevertheless, it is of great interest to see how the characteristic energy and target dependence presently observed will change, particularly for more loosely bound projectiles. The gross dependence on the projectile wave function will be illustrated hopefully by the prior-form DWBA. A calculation using the $E1$ matrix element [Eq. (2)] which is readily evaluated by using Ehrenfest's theorem [32] has been carried out. The projectile is characterized by the binding energy ϵ_d employing the Hulthèn-type wave function $\phi_d(r)=N_0(e^{-\alpha r}-e^{-\beta r})/r$, where $\alpha=\hbar^{-1}\sqrt{\mu_{pn}\epsilon_d}$ and $\beta=6.39\alpha$. Figure 12 shows the energy and target dependence of the double-differential cross section, averaged over the detector solid angles, for each binding energy of 0.2, 2.22, and 20 MeV without any normalization. The result for $\epsilon_d=2.22$ MeV qualitatively agrees with the post-form pure-Coulomb calculation [open symbols in Fig. 8(b)], therefore justifying our attempt. The cross section varies by several orders of magnitude depending on ϵ_d but is not simply scaled by the size of the projectile. The characteristic target dependence, where the cross section tends to be suppressed for heavy targets depending strongly on the incident energy, is found to be even more developed for a deeply bound projectile. The cross section for a very loosely bound projectile on the other hand becomes almost independent of the incident energy, showing a target dependence very close to Z^2. Consequently the effect of distortion is likely to be less pronounced for halo nuclei but critically dependent on the projectile wave function.

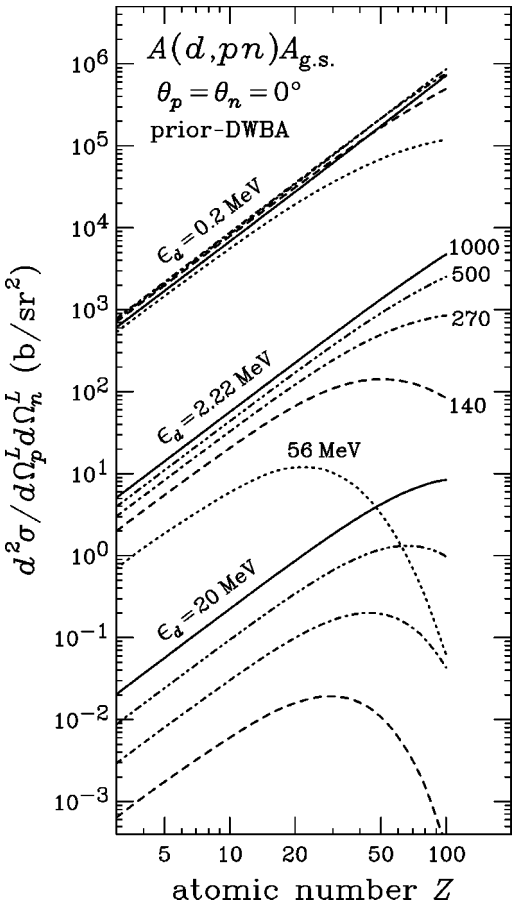

FIG. 12. Dependence of the energy-integrated cross section on the atomic number Z of the target at incident energies of 56, 140, 270, 500, and 1000 MeV for each binding energy ϵ_d of 0.2, 2.22, and 20 MeV calculated by the prior-form DWBA without any normalization.

VI. SUMMARY AND CONCLUSIONS

The elastic breakup of the deuteron has been studied in a kinematically complete measurement at $\theta_p=\theta_n=0°$ and $E_d=140$ MeV and 270 MeV which, together with the previous study at 56 MeV, provides rich information on the energy dependence and the target dependence, ranging from $Z=6$ to 82. The magnitude of the cross sections varies almost in proportion to Z^2 at 270 MeV, indicating the dominance of Coulomb breakup, but tends to be suppressed for heavy targets at lower energies. Likewise, the double-peaked proton-energy spectrum observed in the whole measured region supports the dominance of Coulomb breakup, but becomes asymmetric with increasing target mass and/or decreasing incident energy, although a symmetric shape is expected for the $E1$ transition.

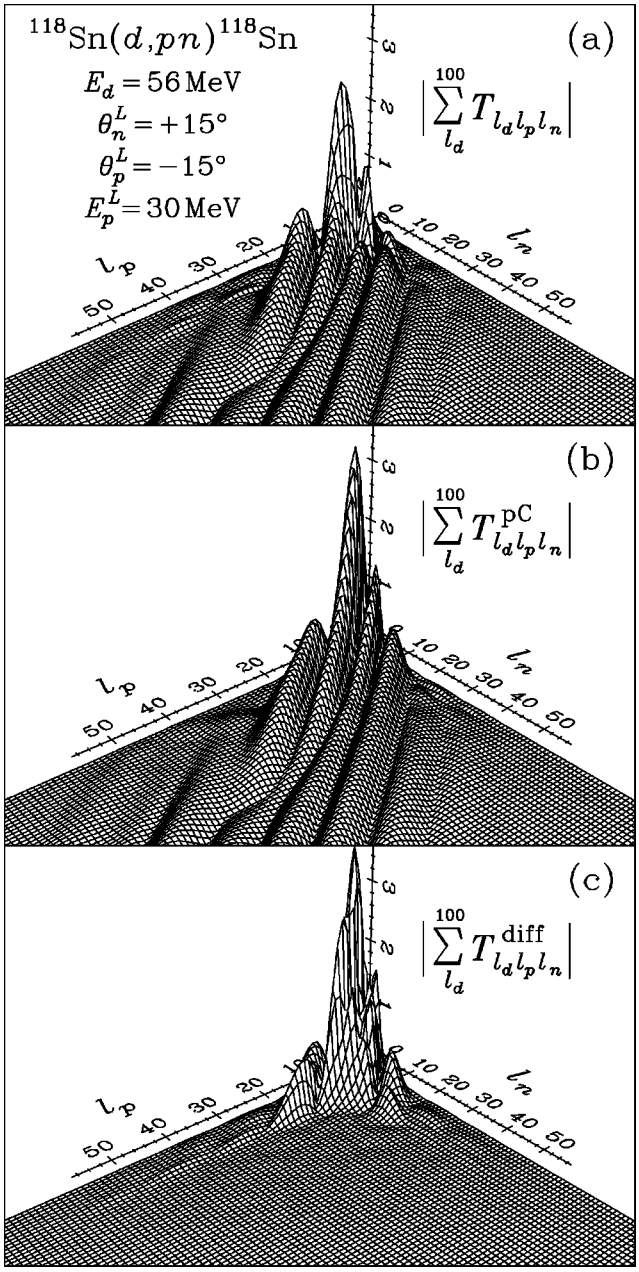

FIG. 13. Amplitudes of the partial T matrices summed over the deuteron partial waves plotted as a function of l_p and l_n for the ^{118}Sn$(d,pn)^{118}$Sn$_{\mathrm{g.s.}}$ reaction at $E_d = 56$ MeV, $\theta_p^L = +15°$, $\theta_n^L = -15°$ (opposite side of the proton in a coplanar geometry), and $E_p^L = 30$ MeV. (a) T_{ZR}, (b) $T_{\mathrm{ZR}}^{\mathrm{pC}}$, and (c) $T_{\mathrm{ZR}}^{\mathrm{diff}}$ correspond to Eqs. (A1), (A2), and (A3), respectively.

Since these observations suggest distortion effects have a large influence at low energies and for high-Z targets, post-form DWBA calculations including nuclear potentials have been carried out. The calculated triple-differential cross sections are found to show very steep and complicated distributions at angles near 0°. It is thus crucial to average the cross section over the detector solid angles to make a comparison with the data. The observed Z dependence is not a simple scaling due to the dominance of the Coulomb breakup, even though it is close to Z^2. The results of calculations including nuclear potentials reproduce the shape of the spectra reasonably well but consistently overestimate the magnitudes of the cross sections by a factor of about 2. The pure-Coulomb calculations better reproduce the magnitude but with poorer agreement in shape. This can be qualitatively understood as a consequence of the improper treatment of the p-n FSI amplitude, the effect of which is enhanced at very forward angles. As we employ the zero-range approximation, the post-form DWBA is not able to predict the dependence on the projectile wave function, which instead has been discussed based on the prior-form DWBA.

In spite of its success at backward angles and lower energies, as well as of its proper treatment of the ejectile distorted waves, which are presumably essential for describing the asymmetric shape of the spectrum, the post-form DWBA fails to fully reproduce the present data. Clearly the reaction is caused mainly by the Coulomb interaction; still, a more advanced theory is needed to obtain its complete understanding. Various reaction problems, such as the post-acceleration effect and the contribution from nuclear breakup, which are vital issues in the analysis of the breakup of halo nuclei, show up in a clear-cut and enhanced way in the deuteron breakup. The present data provide a means for clean and critical tests of models proposed for treating these problems and will hopefully stimulate the development of such theories.

ACKNOWLEDGMENTS

The authors would like to express their appreciation to Dr. Y. Yano, Vice Director of RIKEN, for suggesting the excellent idea of using H_2^+, and to the RIKEN cyclotron crew for their machine operation. They are grateful to Prof. J. Tostevin for valuable discussions on the theoretical treatment of the breakup reaction and for reading the manuscript. They also thank Y. Satou, S. Fujita, T. Ohnishi, T. Nonaka, K. Yakou, S. Fukusaka, and K. Sekiguchi for their collaboration in the elastic-scattering measurement.

APPENDIX

The post-form DWBA calculation has been carried out following the method of Baur and Trautmann [16,33]. Equation (3) is evaluated usually by introducing an approximation $V_{nA} \simeq V_{nB}$, which, however, will be invalid for light targets; besides, the optical potential on the *unbound* target B cannot be deduced experimentally.

The resultant T matrix

$$T_{\mathrm{post}} \simeq \langle \chi_{pA}^{(-)} \chi_{nB}^{(-)} | V_{pn} | \phi_d \chi_{dA}^{(+)} \rangle$$

is further approximated by introducing the zero-range approximation to be

$$T_{\mathrm{ZR}} = D_0 \langle \tilde{\chi}_{pA}^{(-)}(\mathbf{r})\, \tilde{\chi}_{nB}^{(-)}(\gamma \mathbf{r}) | \Lambda(r)\, \tilde{\chi}_{dA}^{(+)}(\mathbf{r}) \rangle, \qquad \text{(A1)}$$

where $\gamma = m_A / m_B$, but including the finite-range correction,

$$\Lambda(r) = \left[1 - \frac{2\mu_{pn}}{\hbar^2} R^2 (V_{pA}(r) + V_{nB}(\gamma r) - V_{dA}(r) - \epsilon_d) \right]^{-1},$$

and the nonlocality corrections for optical potentials,

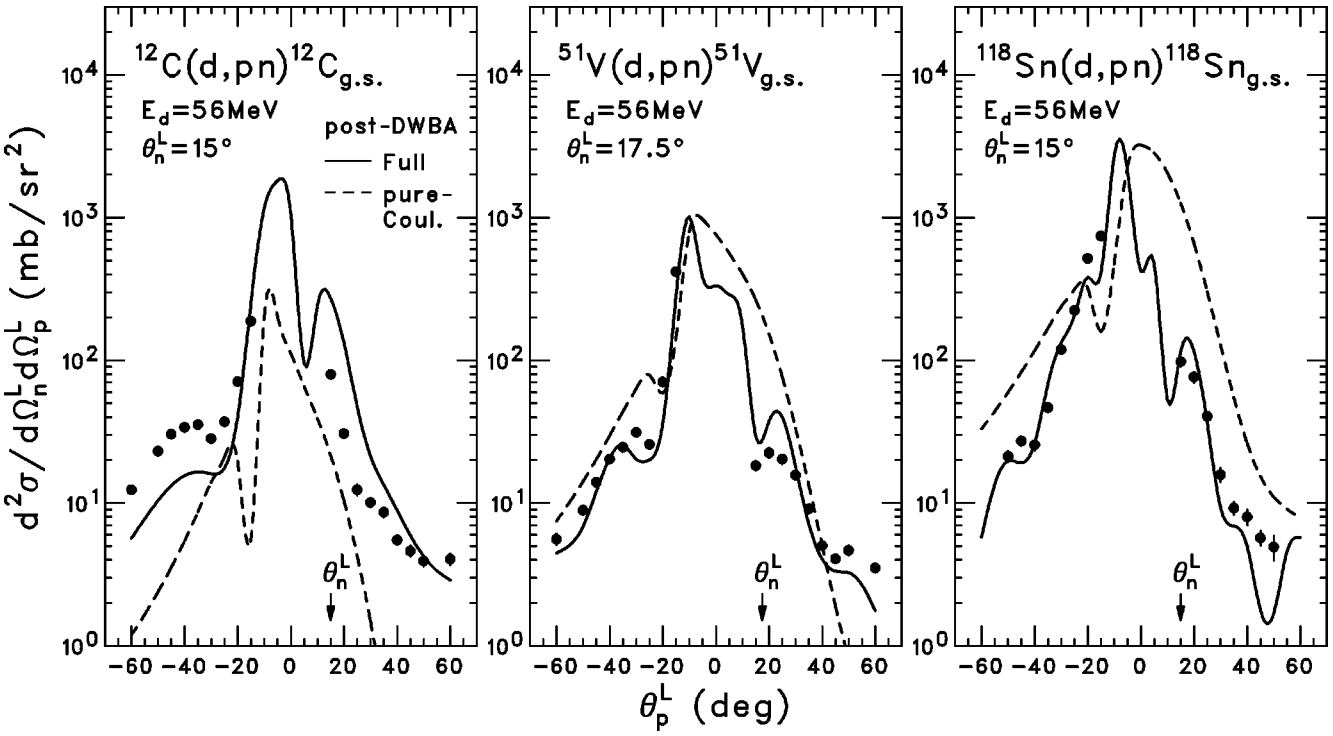

FIG. 14. Energy-integrated cross sections, plotted as a function of the proton angle θ_p^L, for the 56-MeV deuteron breakup from the ^{12}C, ^{51}V, and ^{118}Sn targets while the neutron angles are fixed at $\theta_n^L=15°$, 17.5°, and 15°, respectively (taken from Ref. [36]). The solid and dashed curves are the results (without any normalization) of the post-form DWBA calculations with and without nuclear potentials, respectively.

$$\tilde{\chi}_{iA}^{(\pm)}(\mathbf{r})=\chi_{iA}^{(\pm)}(\mathbf{r})\exp\left[\frac{\beta_i^2}{8}\frac{2\mu_{iA}}{\hbar^2}V_{iA}^N(r)\right].$$

The parameters $D_0=124\,\mathrm{MeV\,fm^{3/2}}$, $R=0.667$ fm, $\beta_{p/n}=0.85$ fm, and $\beta_d=0.54$ fm are used in the present analysis. The validity of the zero-range approximation, however, is a point at issue in the energy region above 100 MeV, where the wave number k_{dA} becomes larger than 3 fm^{-1} and χ_{dA} thus varies considerably within the range of $V_{pn}\phi_d$ which is the order of 1 fm.

Numerical calculations of T_{ZR} still have difficulties in the slow convergence of radial integral, which is solved by the Vincent-Fortune contour integration method [34], and in the long summation over partial waves, which is avoided by introducing the pure-Coulomb T matrix

$$T_{\mathrm{ZR}}^{\mathrm{pC}}=D_0\Lambda^C\langle\chi_{pA}^{C(-)}(\mathbf{r})\,e^{-i\gamma\mathbf{k}_{nB}\cdot\mathbf{r}}|\,\chi_{dA}^{C(+)}(\mathbf{r})\rangle\,, \qquad \text{(A2)}$$

where $\chi_{iA}^{C(\pm)}$ denotes the Coulomb distorted wave. The finite-range correction is reduced to a factor $\Lambda^C(=1.025)$ and there is no nonlocality effect in this case. $T_{\mathrm{ZR}}^{\mathrm{pC}}$ is readily evaluated by using the analytical expression for the bremsstrahlung matrix element [35]. The remaining part

$$T_{\mathrm{ZR}}^{\mathrm{diff}}=T_{\mathrm{ZR}}-T_{\mathrm{ZR}}^{\mathrm{pC}}, \qquad \text{(A3)}$$

which is evaluated by the partial-wave expansion of the distorted waves, converges very rapidly with respect to l_d, l_p, and l_n. As an example, partial T matrices for Eqs. (A1)–(A3) summed over l_d are shown in Fig. 13 as a function of l_p and l_n for the ^{118}Sn$(d,pn)^{118}$Sn$_{\mathrm{g.s.}}$ reaction at 56 MeV in a kinematical condition indicated in the figure. The rapid convergence on the partial waves is a significant advantage over other theoretical treatments particularly for the cases where the Coulomb breakup becomes important. This powerful technique, however, can be applied only to a breakup reaction with one of ejectiles having no charge. In the present analysis, partial waves have been summed up to 50, 70, and 90 ($=l_d^{\max}=l_p^{\max}=l_n^{\max}$) for 56-, 140-, and 270-MeV incident energies, respectively.

In order to recall the remarkable success of the post-form DWBA at backward angles and below 56 MeV, a comparison of the data taken from Ref. [36] with the corresponding calculations is shown in Fig. 14 without any normalization. Our calculation reproduces the data better than the previously presented one in Ref. [37] for heavy targets, partly because we summed up the partial waves up to 50 while the authors in Ref. [37] limited $l_n^{\max}$ to be 20, which, as can be seen from Fig. 13, is not sufficiently large for some kinematical conditions.

[1] G. Baur and M. Weber, Nucl. Phys. **A504**, 352 (1989), and references therein.

[2] L. F. Canto, R. Donangelo, A. Romanelli, and H. Schluz, Phys. Lett. B **318**, 415 (1993); A. Romanelli, L. F. Canto, R. Donangelo, and P. Lotti, Nucl. Phys. **A588**, 71c (1995).

[3] C. A. Bertulani and F. Canto, Nucl. Phys. **A539**, 163 (1992).

[4] H. Esbensen, G. F. Bertsch, and C. A. Bertulani, Nucl. Phys. **A581**, 107 (1995).

[5] T. Kido, K. Yabana, and Y. Suzuki, Phys. Rev. C **53**, 2296 (1996), and references therein.
[6] S. Typel, H. H. Wolter. and G. Baur, Nucl. Phys. **A613**, 147 (1997), and references therein.
[7] P. Banerjee and R. Shyam, Nucl. Phys. **A561**, 112 (1993), and references therein.
[8] H. Okamura, S. Hatori, N. Matsuoka, T. Noro, A. Okihana, H. Sakai, H. M. Shimizu, K. Takeshita, and T. Yamaya, Phys. Lett. B **325**, 308 (1994).
[9] L. F. Canto, R. Donangelo, A. Romanelli, M. S. Hussein, and A. F. R. de Toledo Piza, Phys. Rev. C **55**, R750 (1997).
[10] C. Samanta, S. Mukherjee, R. Kanungo, and D. N. Basu, Phys. Rev. C **53**, 2287 (1996). [It is not clear that the average over the detector solid angles (Sec. IV) is carried out in their analysis considering the extreme overestimate of the cross section. This makes their conclusion on the nuclear-breakup contribution questionable.]
[11] J. A. Tostevin, S. Rugmai, R. C. Johnson, H. Okamura, S. Ishida, N. Sakamoto, H. Otsu, T. Uesaka, T. Wakasa, H. Sakai, T. Niizeki, H. Toyokawa, Y. Tajima, H. Ohnuma, M. Yosoi, K. Hatanaka, and T. Ichihara, Phys. Lett. B **424**, 219 (1998); J. A. Tostevin, S. Rugmai, and R. C. Johnson, Phys. Rev. C **57**, 3225 (1998).
[12] T. Ichihara *et al.*, Nucl. Phys. **A569**, 287c (1994).
[13] H. Okamura, S. Ishida, N. Sakamoto, H. Otsu, T. Uesaka, T. Wakasa, Y. Satou, H. Sakai, T. Niizeki, H. Ohnuma, and T. Ichihara, Nucl. Instrum. Methods Phys. Res. A **406**, 78 (1998).
[14] T. N. Taddeucci *et al.*, Phys. Rev. C **41**, 2548 (1990).
[15] R. A. Cecil, B. D. Anderson, and R. Maddy, Nucl. Instrum. Methods **161**, 439 (1979).
[16] G. Baur and D. Trauttmann, Phys. Rep., Phys. Lett. **25C**, 1525 (1976), and references therein.
[17] N. Austern, Phys. Rev. C **30**, 1130 (1984).
[18] R. C. Johnson and P. J. R. Soper, Phys. Rev. C **1**, 976 (1970).
[19] K. Hosono, M. Kondo, T. Saito, N. Matsuoka, S. Nagamachi, T. Noro, H. Shimizu, S. Kato, K. Okada, K. Ogino, and Y. Kadota, Nucl. Phys. **A343**, 234 (1980).
[20] R. L. Varner, W. J. Thompson, T. L. McAbee, E. J. Ludwig, and T. B. Clegg, Phys. Rep. **201**, 57 (1991).
[21] T. Ohnishi *et al.*, RIKEN Accelerator Progress Report No. **29**, 1996, p. 56; Phys. Lett. B (to be published).
[22] Y. Satou (private communication).
[23] V. Comparat, R. Frascaria, N. Marty, M. Morlet, and A. Willis, Nucl. Phys. **A221**, 403 (1974).
[24] P. Schwandt, H. O. Meyer, W. W. Jacobs, A. D. Bacher, S. E. Vigdor, M. D. Kaitchuck, and T. R. Donoghue, Phys. Rev. C **26**, 55 (1982).
[25] N. Matsuoka, H. Sakai, T. Saito, K. Hosono, M. Kondo, H. Ito, K. Hatanaka, T. Ichihara, A. Okihana, K. Imai, and K. Nisimura, Nucl. Phys. **A455**, 413 (1986).
[26] B. A. Watson, P. P. Singh, and R. E. Segel, Phys. Rev. **182**, 977 (1969).
[27] F. D. Becchetti and G. W. Greenless, Phys. Rev. **182**, 1190 (1969).
[28] J. Raynal, computer code ECIS79 (unpublished).
[29] G. G. Ohlsen, Nucl. Instrum. Methods **37**, 240 (1965).
[30] M. Spraker, B. Ni, J. M. Cameron, E. Jourdan, G. P. A. Berg, D. W. Miller, and T. Rinckel, Nucl. Instrum. Methods Phys. Res. A **394**, 311 (1997).
[31] H. Okamura *et al.*, Phys. Lett. B **227**, 204 (1989).
[32] R. Gold and C. Wong, Phys. Rev. **132**, 2586 (1963).
[33] G. Baur, F. Rösel, and D. Trautmann, Nucl. Phys. **A265**, 101 (1976).
[34] C. M. Vincent and H. T. Fortune, Phys. Rev. C **2**, 782 (1970).
[35] A. Nordsieck, Phys. Rev. **93**, 785 (1954).
[36] N. Matsuoka, K. Hatanaka, T. Saito, T. Itahashi, K. Hosono, A. Shimizu, M. Kondo, F. Ohtani, and O. Cynshi, Nucl. Phys. **A391**, 357 (1982).
[37] G. Baur, R. Shyam, F. Rösel, and D. Trautmann, Phys. Rev. C **28**, 946 (1983).